Article:

Maramizonouz, S., Nadimi, S. orcid.org/0000-0002-0971-7089 and Lewis, R. orcid.org/0000-0002-4300-0540 (2024) CFD-DEM modelling of particle entrainment in wheel–rail interface: a parametric study on train characteristics. Acta Mechanica, 235 (10). pp. 6077-6087. ISSN 0001-5970

https://doi.org/10.1007/s00707-024-04032-8

Acta Mech
https://doi.org/10.1007/s00707-024-04032-8

ORIGINAL PAPER

Sadaf Maramizonouz · Sadegh Nadimi · Roger Lewis

CFD-DEM modelling of particle entrainment in wheel–rail interface: a parametric study on train characteristics

Received: 31 January 2024 / Revised: 17 May 2024 / Accepted: 8 July 2024

Abstract Rail-sanding is employed to improve the train's wheel–rail traction loss in low adhesion conditions. This can significantly impede trains' kinematics, operation, and performance by hindering the train's acceleration and deceleration, resulting in delays and unreliability of transport system as well as causing safety risks and in the worst cases train collisions. Rail-sanding has its own merits in recovering the wheel–rail traction but can result in a sand wastage of more than 80% due to its low sand entrainment efficiency. In this research, computational fluid dynamics is coupled to discrete element modelling to study the behaviour of sand particles during rail-sanding. A parametric study based on the train characteristics, including train velocity, sand flow rate, and the geometry of the sander nozzle, is performed by comparing the entrainment efficiency of the sand particles. It is found that train velocities over 30 m/s result in the entrainment efficiency of almost zero. A moving air layer generated at the wheel–rail interface influences the lower bound of acceptable particle size range. The flow rate and nozzle geometry can be designed to enhance entrainment efficiency.

1 Introduction

The traction[1] between a train's wheel and the rail significantly influences the train's kinematics, operation, and performance throughout both the acceleration and deceleration phases [1–3]. The presence of third-body layers such as water and oil, or leaf contamination bonded to the top surface of the rail can diminish the wheel–rail traction [4–6]. Low traction levels adversely affect the railway transportation in two ways. First, it hinders the train's acceleration which can cause train delays, resulting in the unreliability of transport system. Second, wheel–rail traction loss impedes deceleration generating safety risks, which if not mitigated may cause train collisions [4, 6, 7].

Among the many solutions used to increase the wheel–rail traction to required levels, rail-sanding is the most utilised in which a train-borne system is employed to deposit sand particles into the wheel–rail interface using a jet of compressed air [2, 4–6]. Although this method is successful in recovering the wheel–rail traction, it has its own downsides, one of which is its sand wastage of potentially more than 80% meaning that only less than 20% of the sand particles reach the wheel–rail interface where they can actively increase the traction [1].

Considering that sand has finite resources while needed in numerous applications including computer microchips, construction, and cosmetics, the practicality and sustainability of using sand to increase the wheel–rail traction may present new challenges [8]. The rail-sanding needs to be better understood through

---

[1] In the railway industry "adhesion" is defined as the amount of "traction" present when the wheel–rail contact enters partial slip. In this paper, the terms "traction" and "adhesion" are used interchangeably.

S. Maramizonouz · S. Nadimi (✉)
School of Engineering, Newcastle University, Newcastle upon Tyne NE1 7RU, UK
e-mail: sadegh.nadimi-shahraki@ncl.ac.uk

R. Lewis
Department of Mechanical Engineering, Leonardo Centre for Tribology, University of Sheffield, Sheffield S1 3JD, UK

either experimental investigations or numerical modelling to lessen the sand usage and wastage while boosting the sand entrainment efficiency. This optimised rail-sanding system can help in reducing the safety risks and improving the timeliness of railway transportation taking a step towards a more sustainable railway [2–4].

Experimental investigations of the rail-sanding process are usually performed in controlled environments using either a twin-disc set-up [2, 9, 10], or a full-scale laboratory test rig [1], or by conducting field tests [11]. All these experimental studies, while able to present accurate observations, can be costly and inaccessible for a wider community. Additionally, studying the effects of some specific parameters may not be possible through these experiments.

To enable the investigation of the effects of each variable in a less expensive, and more accessible manner, computational simulations using either finite element method (FEM) [12], or discrete element method (DEM) [13, 14] can be employed to model the rail-sanding process. DEM is more suitable in modelling the dynamics of particulate materials (such as rail-sand) compared to FEM. In addition, both DEM and FEM simulations can also be coupled to computational fluid dynamics (CFD) for more accurate modelling.

In our previous work, DEM simulations of the rail-sanding process were performed for ten case studies where the position of the sander nozzle relative to the wheel and rail was investigated to find the optimum configuration [14]. The ratio of the mass of the sand that passed through the wheel–rail interface to the total amount of sand used was defined as the entrainment efficiency of the sand particles and was estimated by defining a rectangular geometry bin at the wheel–rail interface, counting the number of particles inside it, and dividing that number by the total number of the sand particles generated for the simulation at each time step. The entrainment efficiency and the velocity of the sand particles were exported from the numerical simulation and were compared to and validated by the data already presented by Lewis et al. [1] using a full-scale laboratory wheel–rail test rig. They measured the mass of the sand that remained on the surface of the rail after the wheel passed and divided it by the total mass of the sand used to estimate the entrainment efficiency [1].

In this study, a coupled CFD-DEM model is employed to conduct a parametric study on the train characteristics that affect the rail-sanding process including the velocity of the train, the flow rate of sand deposition, and the geometry of the sander nozzle. The entrainment efficiency of sand particles resulted from each case study is estimated through the data obtained from numerical modelling, and the values are compared to the benchmark case and each other to find the optimum conditions for rail-sanding.

2 Methodology

2.1 Discrete element method

To use the discrete element method for modelling granular materials, one simple but important assumption is that the particles are rigid discrete objects. The dynamic behaviour of the particles is then modelled using Newton's and Euler's laws of translational and rotational motions [15] with the governing equations presented as follows:

$$m_i {}^{d\boldsymbol{v}_i}\!/_{dt} = \sum \boldsymbol{F}_{Ci} + m_i \boldsymbol{g} + \boldsymbol{F}_{Di} \tag{1}$$

$$ {}^{d(\boldsymbol{I}_i \cdot \boldsymbol{\omega}_i)}\!/_{dt} = \sum \boldsymbol{M}_{Ci} \tag{2}$$

where m_i, $\boldsymbol{v}_i$, $\boldsymbol{I}_i$, and $\boldsymbol{\omega}_i$ are the mass, the translational velocity, the moment of inertia, and the rotational velocity of the individual particle, respectively. t is time, and $\boldsymbol{g}$ is the gravitational acceleration. $\boldsymbol{F}_{Ci}$ and $\boldsymbol{M}_{Ci} = \boldsymbol{r}_i \times \boldsymbol{F}_{Ci}$ are the contact force and torque between each particle and its neighbouring particles and walls, $\boldsymbol{r}_i$ is the particle's radius [15], and $\boldsymbol{F}_{Di}$ is the drag force acting on the particle.

For particles' interactions with one another as well as the surfaces of the geometries surrounding them, an appropriate contact model should be utilised. Here, the elastic contact force, i.e. Hertz–Mindlin contact model, is used [15]. This contact model was shown to be accurate enough for the purposes of the current research [14].

2.2 Computational fluid dynamics

The dynamics of the air jet that deposits the sand particles and the air medium surrounding everything is modelled using the Navier–Stokes equations [16]:

$$\nabla.\left(\boldsymbol{U}_f\right) = 0 \tag{3}$$

$$\rho_f\left(\frac{\partial \boldsymbol{U}_f}{\partial t}+\left(\boldsymbol{U}_f\cdot\nabla\right)\boldsymbol{U}_f\right)=-\nabla P+\mu_f\left(\nabla^2\boldsymbol{U}_f\right) \tag{4}$$

where $\boldsymbol{U}_f$, ρ_f, and μ_f are the fluid's velocity vector, density, and viscosity, respectively, and P is the pressure [16].

2.3 CFD-DEM coupling

The discrete element modelling is one-way coupled to the computational fluid dynamic simulations which means that dynamics of the fluid affects the particle behaviour but not vice versa. The CFD-DEM coupling is accomplished through the drag force acting on the sand particles, F_D, which in most cases dictates the majority of the particle dynamics [16, 17]:

$$\boldsymbol{F}_{Di}=\frac{1}{2}\rho_f C_D A\left|\boldsymbol{v}_i-\boldsymbol{U}_f\right|\left(\boldsymbol{v}_i-\boldsymbol{U}_f\right) \tag{5}$$

where C_D is the particle's drag coefficient which is a function of the particle's Reynolds number, Re, and shape, and A is the reference area of the particle.

To couple the CFD model to the DEM simulation in a one-way approach, first, the CFD simulation with known initial and boundary conditions is conducted. After reaching its convergence criteria, the CFD simulation is concluded, and the steady-state velocity field of the fluid can then be exported from the CFD simulations. Then, the fluid velocity field is imported in the DEM model and the Application Programming Interface (API) tool is employed to implement the drag model. The drag model executed through the API is able to estimate the drag force on individual particles using the fluid velocity field obtained from the CFD simulation as well as the dynamic and geometric properties of each particle. During the DEM simulation, at each time step, the drag force is exerted on each particle as an external body force in combination with the other forces the particle experience including their weight and the contact forces. The DEM simulation finishes by reaching the desired end time set for the simulation. The one-way coupling of the CFD-DEM model means that there is only an initial data exchange between the two which is the importing of the air velocity field from the CFD model at the beginning of the DEM simulation.

In our previous research, we compared different models already presented in the literature to estimate various drag models [18]. We found out that the model proposed by Ganser [19] provides acceptable accuracy for different particle geometries [18]. So, here, the Ganser drag model [19] is used which utilises the true sphericity of the particle, Φ_W, defined by Wadell [20] as the ratio of surface area of the volume equivalent sphere to the particle surface area to evaluate the drag coefficient of each particle:

$$C_D=\frac{24K_S}{Re}\left(1+0.1118\left(ReK_N/K_S\right)^{0.6567}\right)+\left(0.4305K_N/\left(1+\frac{3305}{\left(ReK_N/K_S\right)}\right)\right) \tag{6}$$

$$Re=\rho_f\left|\boldsymbol{v}_i-\boldsymbol{U}_f\right|d/\mu_f \tag{7}$$

$$K_N=10^{1.8148\left(-log\Phi_W\right)^{0.5743}} \tag{8}$$

$$K_S=(1/3)+\left((2/3)\sqrt{\Phi_W}\right) \tag{9}$$

where K_S and K_N are called Stokes's and Newton's drag correction factor, respectively, and d is the reference length of the particle which for spherical particulates is the diameter.

2.4 Numerical model set-up

The geometry of the DEM model is built according to the geometry of the full-scale wheel–rail test rig at the Leonardo Centre for Tribology—The University of Sheffield [1]. The wheel has a P8 profile with a ~ 1016 mm diameter, rotating at a 0.098 Rad/s angular velocity. The rail has a 60E1 profile with a ~ 70 mm width and a length of roughly three wheel diameters moving at a set translational velocity. The sander nozzle has a length and a diameter of 150 mm and 25 mm, respectively, and is positioned at a 20° angle relative to the rail [1, 14]. The hopper is filled with a ~ 0.3 kg of spherical sand particles with a size distribution of 30% with 1 mm, 50%

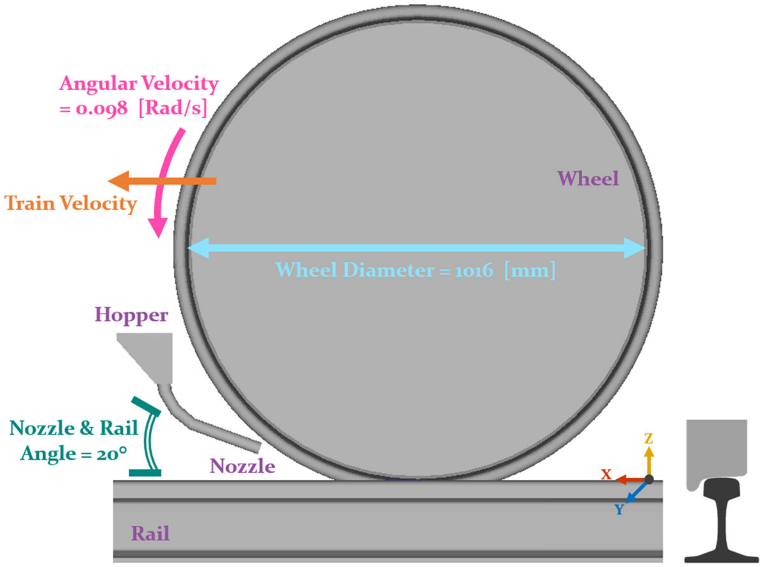

Fig. 1 Geometry layout for the DEM numerical model along with a frontal view of the 60E1 rail and P8 wheel profiles

with 1.2 mm, and 20% with 1.8 mm diameter which corresponds to the range currently proposed in GMRT 2461 from 0.71 mm to 2.8 mm [7]. The particles have a 2600 kg/m^3 density, a 70 GPa Young's modulus, a 0.25 Poisson's ratio, and a 0.5 coefficient of restitution (CoR) on steel [6] which is a physical property implemented in the DEM model to damp the sand particles' bouncing of the steel geometries [21]. Figure 1 presents the details of geometry layout and dynamics of the DEM model.

The DEM modelling software EDEM (version 7.1.0) by Altair is used to carry out the DEM simulations. The time step is set to 10^{-7} which is 20% of the Rayleigh time step. A total number of 21 DEM simulations are reported here.

The geometry of the CFD model is constructed based on the DEM model set-up which includes the sander pipes and the nozzle connecting to a rectangular cuboid with parts of the train wheel and rail cut from it. The boundary conditions are defined as known flow rate at the sander inlet, known ambient pressure at the two outlets, symmetry at the four sides of the rectangular cuboid, and no-slip on all the solid surfaces including cut-outs of the wheel and rail which act as moving walls with a rotational and a translational velocity, respectively. A no-slip boundary condition defines zero fluid velocity relative to the surface of the boundary due to fluid viscosity. Figure 2 presents details of the geometry layout and boundary conditions used for the CFD simulations and the implementation of the CFD data into the DEM model to execute the CFD-DEM coupling.

The CFD simulation is performed using ANSYS FLUENT (version 18.1) with both the time step and convergence criteria set to 10^{-6}. The governing equations of the fluid motion are discretised and solved using the finite volume method (FVM) and the semi-implicit method for pressure-linked equations (SIMPLE), respectively. In order to improve the convergence behaviour of the model, the initial conditions for the CFD simulation are computed by solving the Laplace's equation on a coarse computational mesh based on the inlet and outlet boundary conditions.

Mesh dependency analysis is undertaken to ensure that the simulation results are independent of the resolution of the computational grid, offering desirable accuracy while minimising the computational time and cost. As a result, a mesh resolution of more than 14,000,000 quadratic elements are used for the computational simulation. A total number of 25 CFD simulations including 21 for the parametric study and 4 for mesh dependency analysis have been carried out.

The train's translational velocity, the flow rate of air jet depositing sand onto the rail, and the geometry (cut) of the nozzle tip are the parameters investigated here. The train's translational velocity is applied to the rail.

Table 1 presents the values studied for these three parameters.

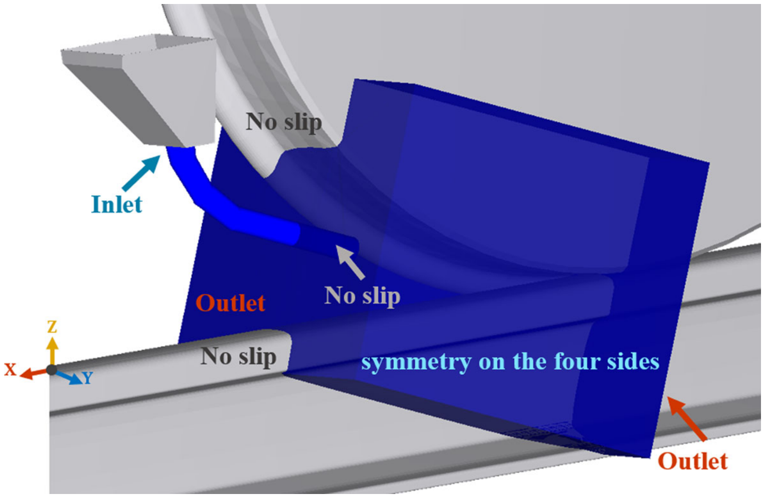

Fig. 2 Geometry layout and boundary conditions for the CFD numerical model, and implementation of the CFD data into DEM simulation to execute the CFD-DEM coupling

Table 1 Values of the input data used for the parametric study

	Parametric study		
	Train velocity (m/s)	Sand flow rate (kg/s)	Nozzle tip cut
Benchmark [14]	0.05	0.0034	Uncut
Train velocity study	5	0.0034	Uncut
	10	0.0034	Uncut
	20	0.0034	Uncut
	30	0.0034	Uncut
	40	0.0034	Uncut
	50	0.0034	Uncut
Sand flow rate study	0.05	0.0005	Uncut
	0.05	0.001	Uncut
	0.05	0.002	Uncut
	0.05	0.004	Uncut
	0.05	0.005	Uncut
	0.05	0.006	Uncut
Nozzle tip study	0.05	0.0034	20° Upward
	0.05	0.0034	25° Upward
	0.05	0.0034	30° Upward
	0.05	0.0034	20° Downward
	0.05	0.0034	25° Downward
	0.05	0.0034	30° Downward
	0.05	0.0034	25° Downward (Length: 50 mm)
	0.05	0.0034	25° Downward (Length: 150 mm)

3 Results and discussion

As stated in the Introduction, the entrainment efficiency is calculated based on the number of particles reaching a virtual rectangular bin in the wheel–rail interface divided by the total number of particles. In our previous study, it was shown that the entrainment efficiency of the sand particles is dependent on the size and location of this rectangular bin [14]. In the current work, the same geometry bin is used at the same location to estimate the entrainment efficiency for all case studies, and the results and trends are comparable.

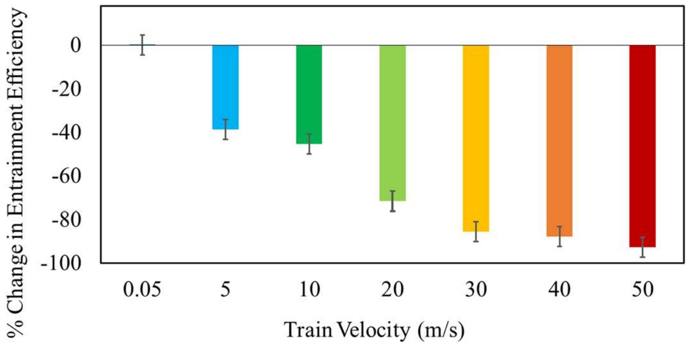

Fig. 3 Percentage change in the entrainment efficiency of the rail-sanding for six values of train velocity compared to the benchmark case of 0.05 m/s train velocity which can be considered as almost stationary

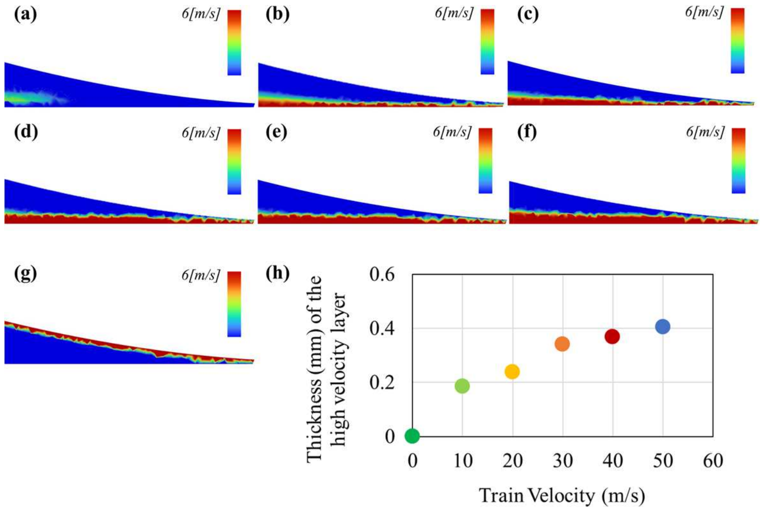

Fig. 4 Close up of the air velocity field at the wheel–rail interface at translational velocity of **a** 0.05 m/s, **b** 10 m/s, **c** 20 m/s, **d** 30 m/s, **e** 40 m/s, **f** 50 m/s applied to the rail, **g** 30 m/s applied to the wheel, and **h** a graph showing the thickness of the high velocity layer vs. the train velocity

3.1 Train velocity

Figure 3 shows the percentage change in the entrainment efficiency of the rail-sanding for six train velocity values compared to the benchmark case with train velocity of 0.05 m/s which can be assumed as almost stationary. It can be seen that as the train velocity increases, the entrainment efficiency of the rail-sanding decreases. When the train velocity exceeds 30 m/s, the entrainment efficiency reduces to near zero. It means that at high velocities, there is only a little amount of sand deposited at the wheel–rail interface. This can result in train safety issues due to loss of traction at higher velocities.

Figure 4(a)–(f) presents a close-up of the air velocity field at the wheel–rail interface at six different train velocities applied to the rail. For comparison purposes, another case study has been investigated where the train velocity of 30 m/s is applied to the wheel and the result presented in Fig. 4(g).

It can be seen that a moving air layer forms at the wheel–rail interface and its thickness increases with train velocity as shown in Fig. 4h. At high train velocities, the thickness of this layer can increase up to 0.4 mm which means that at higher train velocities, entrainment will be challenging for particles smaller than 0.4 mm. This results in the introduction of an acceptable minimum particle size which is in line with the minimum particle size of 0.71 mm proposed in GMRT 2461 [7].

It is worth noting that while in these studies the train velocity is applied to the rail, a similar layer will form at the wheel–rail interface when the velocity is applied to the wheel (Fig. 4g), creating the same condition at the wheel–rail interface. So, similar remark regarding the minimum particle size can be established.

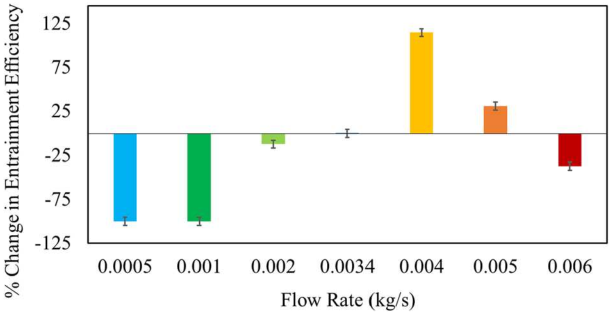

Fig. 5 Percentage change in the entrainment efficiency of the rail-sanding for six values of sand flow rate compared to the benchmark case of 0.0034 kg/s sand flow rate

3.2 Sand flow rate

Figure 5 shows the percentage change in the entrainment efficiency of the rail-sanding for six sand flow rate values compared to the benchmark case with a flow rate of 0.0034 kg/s. It can be seen that for flow rates lower than the benchmark, the entrainment efficiency of the rail-sanding decreases as the flow rate decreases. For flow rates higher than the benchmark, the entrainment efficiency of the rail-sanding is also higher than that of the benchmark for 0.004 kg/s and 0.005 kg/s; however, as the flow rate increases to 0.006 kg/s, the entrainment efficiency of the rail-sanding decreases. So, each sander configuration can be optimised at a certain flow rate.

One approach to study the flow of particles through air to see whether they follow the streamlines of the fluid flow, or their inertia dominates their trajectories, is to investigate their Stokes number defined as [16]:

$$Stk = t_p \boldsymbol{U}_f / d \tag{10}$$

where t_p is the particle's relaxation time. If $Stk \ll 1$ or $Stk \gg 1$, the particle's trajectory is dictated by the flow streamlines or the particle's own inertia, respectively [16]. Here, for the particles with diameters of 1 mm, 1.2 mm, and 1.8 mm, the Stokes number is calculated to be within the same order of magnitude with the values between 1 and 9 for different flow rates including the benchmark case. It can then be concluded that as the air flow inside the sander moves the stationary particles out of the hopper, through the sander nozzle and into the wheel–rail interface, it affects the particles' trajectories to an extent. However, the particles also experience gravity due to their mass, multiple inter-particle collisions, and collisions with sander walls which contribute to the divergence of the particles' trajectories from the flow streamlines especially after exiting the nozzle and colliding with the rail.

3.3 Sander nozzle

The sander nozzle plays a role in the efficiency of the particles' entrainment during rail-sanding. The sander is usually a cylindrical tube (made of steel or rubber) and for the benchmark case here is positioned at 60 mm above the rail and 320 mm from the wheel–rail interface nip. In order to investigate the effect of the geometry of the sander, its nozzle can be cut with an angle in either an upward or a downward configuration. Here, six different sander geometries with angles of 20°, 25°, and 30° in both upward and downward configurations are investigated in the simulations and presented in Fig. 6(a-1)–(c-2). To study the effect of sander placement, two cases using sanders with a 25° downward cut positioned at 50 mm above the rail and 280 mm from the nip and 10 mm above the rail and 190 mm from the nip are investigated and shown in Fig. 6(d-1) and (e-1), respectively.

Figure 7 shows the percentage change in the entrainment efficiency of the rail-sanding for six different sander nozzle cuts (Fig. 6(a-1) to (c-2)) and two different sander placements (Fig. 6(d-1) and (e-1)) compared to the benchmark case of an uncut cylindrical sander nozzle. It can be seen that for the sanders with the same placement, cutting the sander tip in upward configurations results in the decrease in or no change in the entrainment efficiency. Cutting the sander tip in downward configurations increases the entrainment efficiency especially with a 30° angle. Comparing the two cases of sanders closer to the rail with distances of 50 mm (Fig. 6(d-1)) and 10 mm (Fig. 6(e-1)) with the same 25° downward cut to the benchmark sander (Fig. 6(b-1)) shows that placing the sander closer to the rail increases the entrainment efficiency of the particles.

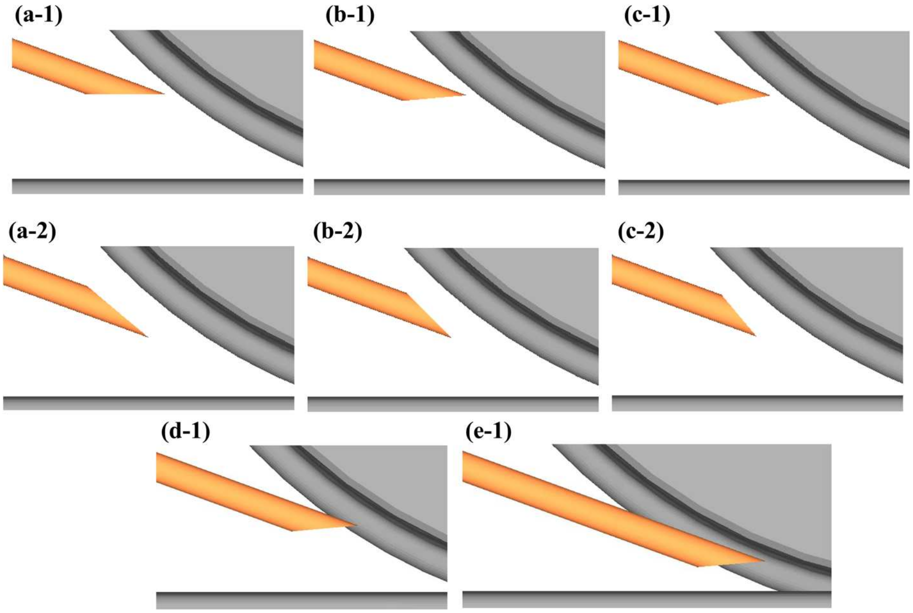

Fig. 6 Six sander nozzle tip geometries cut with an angle of **a** 20°, **b** 25°, **c** 30°, a tip with 25° cut and positioned at **d** 50 mm, and **e** 10 mm above the rail and with **(1)** a downward, and **(2)** an upward configuration

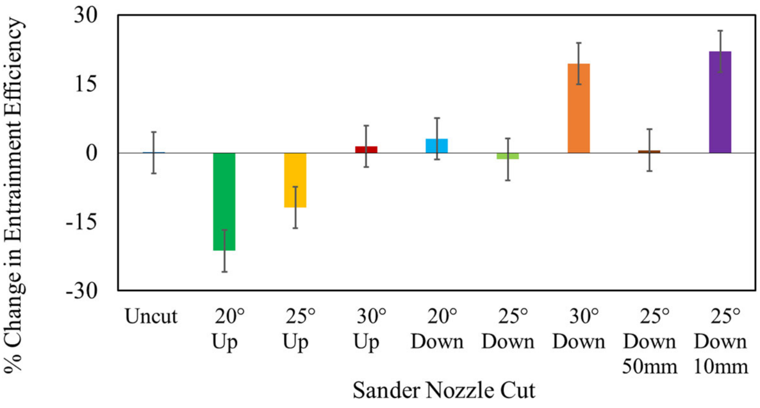

Fig. 7 Percentage change in the entrainment efficiency of the rail-sanding for six sander nozzle configurations and placements compared to the benchmark case of uncut cylindrical sander nozzle

The value of Stokes number remains similar to the benchmark case for all the case studies with different sander cuts and placements. Comparable values of the Stokes number shows that while the particles' trajectories are influenced by both the air flow inside the sander and the inertial forces (gravity and contact forces) the particles experience, these effects are similar for all nine sander configurations including the uncut sander. So, the difference between the particle entrainment efficiencies can be attributed to sander nozzle geometry.

Figure 8 presents the trajectories of a selection of particles as they exit the nozzle and reach the wheel–rail interface at a set time step coloured by their velocities for the three cases of (a) uncut sander, sander cut with an angle of (b) 30° upward, (c) 30° downward, and (d) 25° downward placed 10 mm above the rail. Downward configurations of the sander generally direct higher number of particles towards the top surface of the rail creating a relatively thicker sand layer. This can result in an increase in the particle entrainment efficiency as more particles can reach the wheel–rail interface. For sanders with different lengths shown, as the sander length increases, it can direct all the particles towards the wheel–rail interface for a longer duration. This results in an enhancement in the particles' entrainment efficiency due to the shorter distance the particles need to travel on their own before reaching the wheel–rail interface hence having less time to diverge from correct entrainment trajectories.

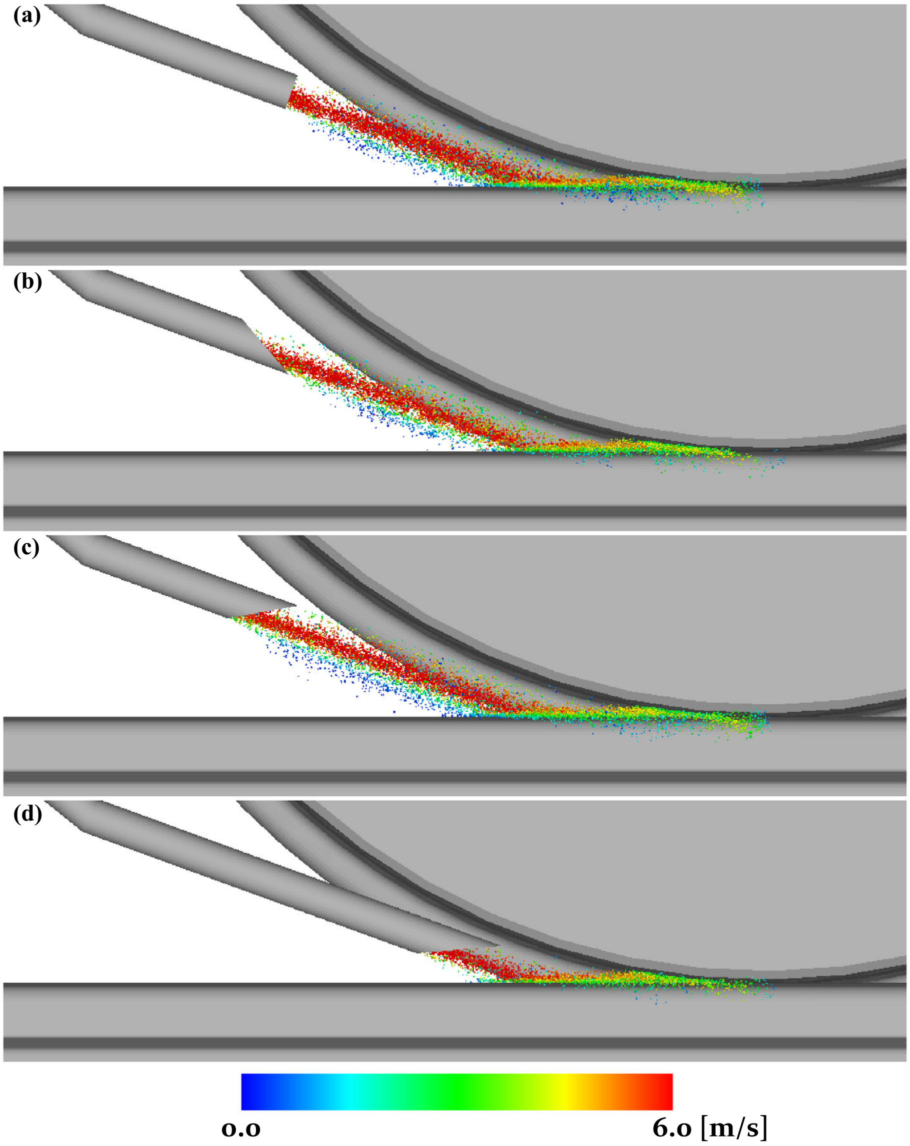

Fig. 8 Particle trajectories at a set time step coloured by their velocities for sander nozzle tip configurations of **a** uncut, cut with an angle of **b** 30° upward, **c** 30° downward, and **d** 25° downward placed 10 mm above the rail

4 Conclusions

In this research, numerical simulations using CFD-DEM coupling were performed to model the rail-sanding process and present a parametric study on the train characteristics. The particle entrainment efficiency obtained from the simulations was compared to better understand the effect of each parameter. It was shown that increasing the train velocity reduces the entrainment efficiency of the sand particles with a near 100% decrease for train velocities of over 30 m/s. Additionally, due to the formation of a moving air layer with a thickness of ~ 0.4 mm at the wheel–rail interface, particles with a size smaller than 0.4 mm have a very low chance of entrainment, especially at higher velocities which was shown to dramatically reduce the entrainment efficiency. It was presented that the changes in sanding flow rate affect the entrainment efficiency with flow rates lower than the benchmark decreasing the entrainment efficiency while flow rates higher than the benchmark increasing the entrainment efficiency. It was found that the entrainment efficiency is highest for an uncut sander, while the sanders with downward cuts perform better than the ones with upward cuts. Comparing three cases of sanders with downward cuts of the same angle but with different lengths showed that as the sander length increases, the entrainment efficiency of the particles increases as well. This is due to the shorter distance the particles need to travel to reach the wheel–rail interface which results in them having less time to diverge from the correct entrainment path.

Acknowledgements This work was funded by the UK Engineering and Physical Sciences Research Council (EPSRC) grant No. EP/V053655/1 RAILSANDING—Modelling Particle Behaviour in the Wheel-Rail Interface. The authors would like to acknowledge the partnership with and the support received from Altair Engineering Inc.

Author contributions SM contributed to conceptualisation, methodology, validation, formal analysis, investigation, data curation, visualisation, writing—original draft, and writing—review and editing, and provided software. SN was involved in conceptualisation, methodology, validation, resources, supervision, project administration, funding acquisition, and writing—review and editing. RL contributed to conceptualisation, resources, supervision, and writing—review and editing. All authors read and approved the final manuscript.

Funding This research was supported by Engineering and Physical Sciences Research Council (Grant No. EP/V053655/1).

Declarations

Conflict of interest The authors declare that they have no known competing financial interests or personal relationships that could influence the work reported in this paper.

References

1. Lewis, S., Riley, S., Fletcher, D., Lewis, R.: Optimisation of a railway sanding system for optimal grain entrainment into the wheel-rail contact. Proc Inst Mech Eng, Part F: J Rail Rapid Transit **232**(1), 43–62 (2018). https://doi.org/10.1177/0954409716656220
2. Arias-Cuevas, O., Li, Z., Lewis, R.: A laboratory investigation on the influence of the particle size and slip during sanding on the adhesion and wear in the wheel-rail contact. Wear **271**(1–2), 14–24 (2011). https://doi.org/10.1016/j.wear.2010.10.050
3. Skipper, W., Chalisey, A., Lewis, R.: A review of railway sanding system research: Wheel/rail isolation, damage, and particle application. Proc Inst Mech Eng, Part F: J Rail Rapid Transit **234**(6), 567–583 (2020)
4. Skipper, W.A., Chalisey, A., Lewis, R.: A review of railway sanding system research: adhesion restoration and leaf layer removal. Tribol-Mater, Surf Interfaces **12**(4), 237–251 (2018)
5. Cooper P (1972) An investigation into the relationship between the particle size and the frictional performance of sand (IM-ADH-011), British Rail Research. Available: https://www.sparkrail.org/Lists/Records/DispForm.aspx?ID=10483
6. Skipper, W., Nadimi, S., Chalisey, A., Lewis, R.: Particle characterisation of rail sands for understanding tribological behaviour. Wear **432**, 202960 (2019)
7. GMRT2461 Sanding Equipment (Issue 3), R. S. a. S. Board, 2018
8. Maramizonouz, S., Nadimi, S., Skipper, W., Lewis, R.: Characterisation and tribological testing of recycled crushed glass as an alternative rail sand. Proc Inst Mech Eng, Part F J Rail Rapid Transit (2023). https://doi.org/10.1177/09544097231164716
9. Lewis, R., Dwyer-Joyce, R.: Wear at the wheel/rail interface when sanding is used to increase adhesion. Proc Inst Mech Eng, Part F: J Rail Rapid Transit **220**(1), 29–41 (2006)
10. Wang, C., et al.: Adhesion and damage characteristics of wheel/rail using different mineral particles as adhesion enhancers. Wear **477**, 203796 (2021)
11. Arias-Cuevas, O., Li, Z.: Field investigations into the performance of magnetic track brakes of an electrical multiple unit against slippery tracks. Part 1: adhesion improvement. Proc Inst Mech Eng, Part F: J Rail Rapid Transit **225**(6), 613–636 (2011)
12. F. Duan (2015). Numerical tribology of the wheel-rail contact: Application to corrugation defect," INSA de Lyon
13. Descartes, S., et al.: A new mechanical–electrical approach to the wheel-rail contact. Wear **265**(9–10), 1408–1416 (2008)
14. Maramizonouz, S., Nadimi, S., Skipper, W.A., Lewis, S.R., Lewis, R.: Numerical modelling of particle entrainment in the wheel-rail interface. Comput Part Mech **10**(6), 2009–2019 (2023). https://doi.org/10.1007/s40571-023-00603-z
15. Thornton C (2015) "Granular Dynamics, Contact Mechanics and Particle System Simulations," *A DEM study. Particle Technology Series,* 24
16. White, F. M.: Fluid mechanics. McGraw Hill (2011)

17. Michaelides, E. Crowe, C. T. Schwarzkopf, J. D.: Schwarzkopf, Multiphase Flow Handbook. CRC Press (2016)
18. Maramizonouz, S., Nadimi, S.: Drag force acting on ellipsoidal particles with different shape characteristics. Powder Technol **412**, 117964 (2022). https://doi.org/10.1016/j.powtec.2022.117964
19. Ganser, G.H.: A rational approach to drag prediction of spherical and nonspherical particles. Powder Technol **77**(2), 143–152 (1993)
20. Wadell, H.: Volume, shape, and roundness of rock particles. J Geol **40**(5), 443–451 (1932)
21. Tsuji, Y., Tanaka, T., Ishida, T.: Lagrangian numerical simulation of plug flow of cohesionless particles in a horizontal pipe. Powder Technol **71**(3), 239–250 (1992). https://doi.org/10.1016/0032-5910(92)88030-L